ELSEVIER

Physica C 368 (2002) 1–9

PHYSICA C

www.elsevier.com/locate/physc

Magnetoencephalography: the art of finding a needle in a haystack

J. Vrba *

CTF Systems Inc., A Subsidiary of VSM MedTech Ltd., 15-1750 McLean Ave., Port Coquitlam, B.C., Canada V3C 1M9

Abstract

The brain's magnetic signals are much weaker than the magnetic disturbances inside the typical commercial magnetically-shielded room. Magnetic noise arises from far-field environmental sources (power lines, vehicles, etc.) and from near-field biological sources (electrically active tissues, such as muscle, heart, unwanted brain signals, etc.). Some form of inverse solution is generally used to solve for the sources that account for the MEG measurements. However, the inversion problem is non-unique and ill defined. Given the large amounts of noise and the non-uniqueness, how can MEG inversion succeed? One must provide methods for efficient attenuation of environmental noise, combined with MEG localization methods that are robust against the background clutter. Noise cancellation methods will be reviewed, and it will be shown that a combination of synthetic gradiometers, adaptive signal processing, and moderately shielded rooms can provide environmental noise attenuation in excess of 10^7. Two types of MEG signal analysis techniques will be discussed: those depending solely on prior noise cancellation (e.g., equivalent current dipole fit and minimum norm), and those intrinsically providing additional cancellation of far and near field noise (e.g., beamformers). The principles and behavior of beamformers for variations in signal and noise will be explained. Several beamformer classes will be discussed, and the presentation will conclude with examples of their clinical applications.

Keywords: Magnetoencephalography; Synthetic gradiometers; Beamformers

1. Introduction

Ionic currents associated with a functioning brain produce measurable electric and magnetic fields. The human brain electrical potentials were first measured in 1929 [1] using vacuum tube amplifiers. The magnetic field of the brain (MEG) was first measured in 1968 [2] by room temperature coils. The MEG signal resolution was dramatically improved with the advent of SQUID sensors [3,4], which were first used for detection of MEG in 1972 [5]. Following this pioneering work, the number of MEG channels was gradually increased in order to increase the coverage of the head. This led to the introduction of whole-cortex systems in 1992 [6,7]. Modern whole-cortex MEG systems have several hundred primary channels and are produced commercially.[1] An example of a 275 channel

* Tel.: +1-604-941-8561; fax: +1-604-941-8565.
E-mail address: jvrba@ctf.com (J. Vrba).

[1] CTF Systems Inc., A subsidiary of VSM MedTech Ltd., 15-1750 McLean Ave., Port Coquitlam, B.C., Canada V3C 1M9; 4D Neuroimaging Inc., 9727 Pacific Heights Blvd., San Diego, CA 92121-3719; Yokogawa Electric Corporation, MEG Business Center, Musashino-city, Tokyo, 180-8750, Japan; Advanced Technologies Biomagnetics S.r.l., Via Martiri di Pietransieri 2, 65129 Pescara, Italy.

0921-4534/01/$ - see front matter
PII: S0921-4534(01)01131-5

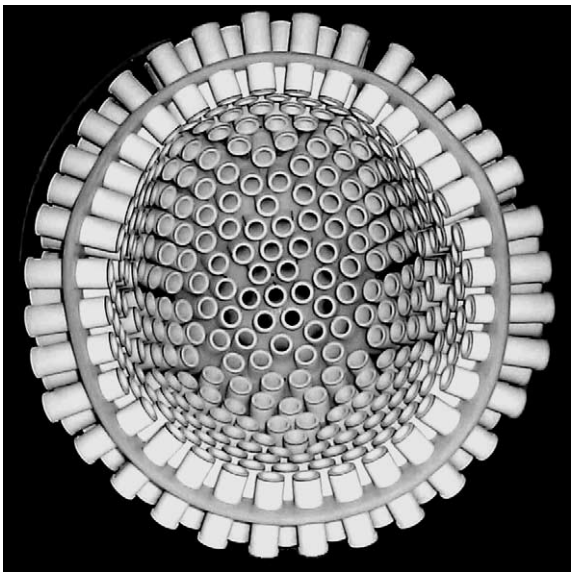

Fig. 1. Example of MEG sensor array, 275 radial gradiometers with 5 cm baseline.

whole-cortex MEG array is shown in Fig. 1.[2] Commercial MEG systems are reliable, easy to operate and their sensor white noise levels are typically <10 fT rms/$\sqrt{}$Hz (usually about 5 fT rms/$\sqrt{}$Hz). This noise level is sufficiently low for the majority of MEG measurements.

MEG instrumentation has also been extended to measure fetal brain signals (fMEG) [8]. The fMEG dewar is horizontal and the sensor array is shaped to cover the mother's abdominal surface from the perineum to the top of the uterus.

The present commercial MEG systems utilize low T_C SQUIDs operated at liquid He temperatures. High T_C SQUIDs are not used for the commercial systems because their reliability, reproducibility, and noise levels have not yet attained the levels available with low T_C sensors.

This paper is organized as follows: challenges faced by MEG are surveyed in Section 2. A description of methods for noise cancellation and MEG source localization is given in Section 3. For lack of space, only the higher-order synthetic gradiometers and beamformers are explained in a greater detail. Examples of MEG data analysis by beamformers is shown in Section 4 and the paper is concluded in Section 5.

2. MEG challenges

MEG fields are small, in the range from 10 fT to about 1 pT, and frequencies from less than 0.1 Hz to about 1 kHz [9–11]. Even though the MEG fields are usually measured inside magnetically shielded rooms, the environmental magnetic noise still dominates. A comparison of typical magnitudes of the environmental noise and biomagnetic fields is shown in Fig. 2. It is immediately obvious that the environmental noise is many orders of magnitude larger than the MEG fields, even if the shielded room attenuation is taken into account (see Section 3.1).

In addition to the environmental noise, the MEG sensors are also exposed to unwanted signals from electrically active body tissues (e.g., muscles, heart, parts of the brain, eyeblinks, etc.). For radial gradiometers, the background brain activity produces about 30 fT rms/$\sqrt{}$Hz correlated

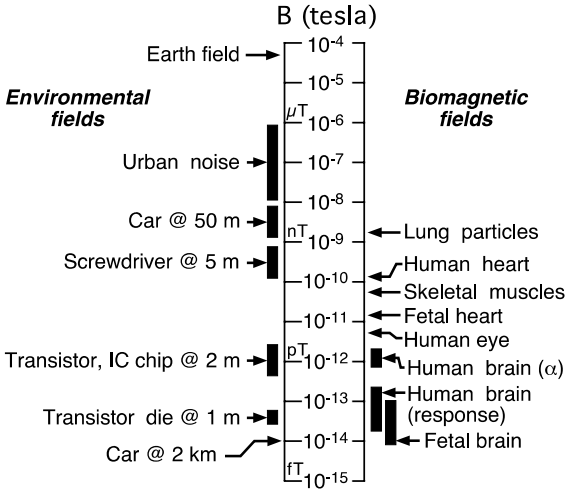

Fig. 2. Comparison of biomagnetic and unshielded environmental fields, logarithmic scale.

[2] CTF Systems Inc., A Subsidiary of VSM MedTech Ltd., 15-1750 McLean Ave, Port Coquitlam, B.C., Canada, V3C 1M9.

noise at frequencies below about 50 Hz [7], i.e., about five to six times larger than the white noise level. Cardiac activity can contribute up to 1 pT to the MEG signals and up to 10 pT to the fMEG signals, i.e., 100–1000 times larger than the signals of interest.

The MEG measurements are generally interpreted by inverse solution methods to obtain the current distributions within the brain. The inversion problem is, however, non-unique [12], i.e., there are many current configurations which can give rise to the same field patterns. In addition, there are fewer than 1000 sensors, while there are roughly 10^{14} synaptic connections within the human cortex. Even if the neurons within each cortical column were synchronized and acted as one source, the problem would remain highly undetermined. To make the inversion possible, various simplifications or mathematical models must be made. However, even then, the problem is often ill defined and extraction of the current distribution is difficult.

In summary, we seek methods to interpret minute MEG signals which coexist with many orders of magnitude larger noise. It is like looking for the proverbial needle in a haystack. How is it possible to succeed and obtain meaningful results? The answer is to apply efficient noise cancellation and use MEG inversion techniques which not only contribute to noise cancellation, but also exhibit good resolution for multiple sources. For event-related experiments, the noise is attenuated by averaging and is often adequately low for successful MEG inversion. However, when averaging is not possible and spontaneous MEG signals are measured, the noise cancellation and elimination of the unwanted brain signals and other body-generated noise becomes extremely important. Methods for noise cancellation and MEG source localization are listed in Table 1.

Table 1 (panel a) contains methods used only for noise cancellation. The methods in Table 1 (panel b) provide MEG source localization, but require careful noise elimination by the methods in Table 1 (panel a). Finally, the methods listed in Table 1 (panel c) provide both noise cancellation and MEG source localization.

Table 1
Noise cancellation and MEG source localization methods

(a) Noise cancellation
- Shielding
- Active shielding
- Synthetic methods
  Synthetic gradiometers
  Adaptive methods

(b) MEG source localizations which critically depend on noise cancellation
- Dipoles
- Minimum norms
- Bayesian inference (see e.g., recent Ref. [13])

(c) Noise cancellation and MEG source localization
- Beamformers (SAM, LCMV, eigenspace, SSP)
- Multiple signal classification
- Principal component analysis
- Independent component analysis
- Non-linear dynamics

3. MEG data analysis methods

Methods listed in Table 1 will be discussed with special emphasis on the synthetic higher-order gradiometers and beamformers.

3.1. Environmental noise cancellation

Shielding is the most straightforward noise elimination method. The simplest shielding can be accomplished by eddy currents using a thick layer of high-conductivity metal [14]. Since such shielding is not effective at low frequencies, it is supplemented by one or more μ-metal layers. Shields for biomagnetism usually exhibit a moderate low frequency attenuation of less than 100 (e.g. Ref. [15]). High attenuation μ-metal rooms with low frequency attenuation of 10^4 or more have also been constructed. An enclosure having seven μ-metal layers and with active shielding achieves field noise attenuation of about 2×10^7 [16]. Low frequency attenuation of nearly 10^8 has been achieved with a high T_C superconducting whole-body shield [17].

Environmental noise can be effectively cancelled using gradiometers, which attenuate noise from distant sources, while having only a small effect on signals from near field MEG sources. Hardware

gradiometers of up to third order have been constructed [18]. However, sensors higher than first order are large, have large inductances and are therefore difficult to match to planar SQUIDs. Commercial MEG systems use either magnetometers or first-order gradiometers as primary sensors, and when required the higher-order gradiometer response is obtained synthetically [18].

Gradiometer synthesis is illustrated in Fig. 3 using an example of a magnetometer sensor and a vector magnetometer reference [18–20]. The primary magnetometer detects the projection of the magnetic field to the coil vector, $\boldsymbol{p}$, as $\sigma = \alpha_s(\boldsymbol{p}\boldsymbol{B}_o)$, where α_s is the magnetometer gain, and $\boldsymbol{B}_o$ is the magnetic field vector at the magnetometer center. The reference magnetometers measure three orthogonal projections of the field $\boldsymbol{B}$ at the reference center, $\boldsymbol{r}_k = \alpha_r B_k$, $k = 1$–3, where $\boldsymbol{r}$ is the vector of the measured reference field, and the reference gains, α_r, are assumed to be equal. A first-order gradiometer is synthesized by projecting the reference output to the vector $\boldsymbol{p}$ and subtracting it from the magnetometer output

$$g^{(1)} = \sigma - \frac{\alpha_s}{\alpha_r}(\boldsymbol{p}\cdot\boldsymbol{r}) = \alpha_s \boldsymbol{p}\cdot(\boldsymbol{B}_o - \boldsymbol{B}) = \boldsymbol{p}\boldsymbol{G}\boldsymbol{b}_1 \qquad (1)$$

where $\boldsymbol{G}$ is first gradient tensor, and $\boldsymbol{b}_1$ is the first-order gradiometer baseline vector. The first-order gradiometer output can also be expressed as a projection of the first gradient tensor to the coil orientation and baseline vectors. If these vectors have general orientations, the first order synthetic gradiometer in Eq. (1) is a linear combination of the first gradient tensor components.

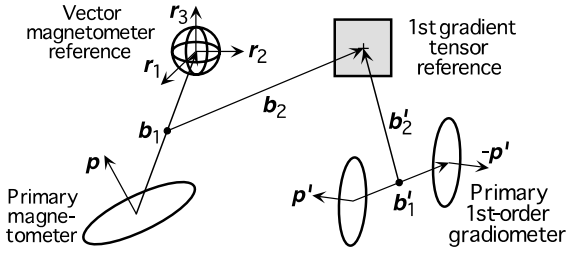

Fig. 3. Gradiometer synthesis. A primary magnetometer can be used to synthesize a first-order gradiometer (left). A primary hardware first-order gradiometer or primary magnetometer can be used to synthesize a second-order gradiometer (right) [18].

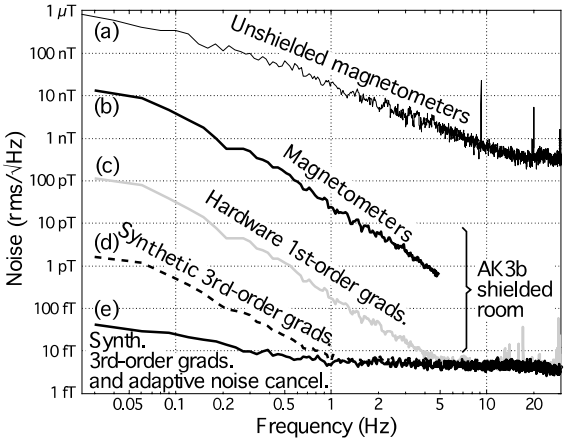

Fig. 4. Reduction of environmental noise by a moderately shielded room [15], synthetic gradiometers, and adaptive methods (see text). MEG site in Toronto.

A second-order gradiometer can be synthesized either from a synthetic or a hardware first-order gradiometer, and a reference first-order tensor gradiometer, Fig. 3 [18]. The procedure is similar to that for the first-order gradiometer synthesis and the result is $g^{(2)} = \boldsymbol{p}\boldsymbol{G}^{(2)}\boldsymbol{b}_1\boldsymbol{b}_2$, where $\boldsymbol{G}^{(2)}$ is the second gradient tensor and $\boldsymbol{b}_2$ is second-order gradiometer baseline. If the synthesis in Fig. 3 is started from a hardware first-order gradiometer, then $\boldsymbol{p}'$, $\boldsymbol{b}'_1$, and $\boldsymbol{b}'_2$ should be used instead. Synthesis of higher-order gradiometers follows similar principles.

The performance of a synthetic third-order gradiometer is illustrated in Fig. 4. The upper trace (a) shows the magnetic field noise outside a shielded room and the trace (b) shows the field noise after attenuation by the shielded room. The difference of the two magnetometer trace slopes is caused by the frequency dependent eddy current shield which is part of the room. Hardware first-order radial gradiometers with 5 cm baseline reduce the noise by nearly a factor of 100 (c) and synthesis of a third-order gradiometer (d) reduces the noise by almost another factor of 100. Thus at low frequencies, the combination of the moderately shielded room and synthetic third-order gradiometers reduces the noise by about a factor of 10^6. Note that the frequency lines detected by first-order gradiometers above 10 Hz are eliminated by the third-order gradiometer.

Adaptive methods can also be applied in addition to the use of third-order gradiometers [18]. They can incorporate the same references as the gradiometers, but their coefficients are explicitly computed to minimize correlated noise. The combination of all methods in Fig. 4 achieves low frequency attenuation of $>10^7$ (comparable to that obtained by high attenuation μ-metal rooms [16]). Prerequisites for such effective noise cancellation are a large dynamic range and good linearity for the detection system.

The adaptive methods perform well if the noise character is not changing. However, if the noise character or the dewar orientation change, new adaptive coefficients must be determined. In contrast, the synthetic gradiometer coefficients are constant, independent of noise character or dewar orientation. The noise cancellation by synthetic gradiometers and adaptive methods is reversible and can be carried out either in real-time or in post-processing.

The field attenuation of shielded rooms can be augmented by active shielding, e.g., [21,22], which consists of reference magnetometers and compensating coils connected in a negative feedback loop. Field attenuation by a factor of 100 or more can be achieved. However, the cancellation field is non-uniform and degrades the performance of synthetic gradiometers.

3.2. MEG inversion methods which depend on noise cancellation

The methods listed in Table 1 (panel b) depend critically on good noise cancellation. The equivalent current dipole (ECD) [10,23] is the oldest and most frequently used model for brain source activity. The ECD analysis proceeds by guessing the number of dipoles and their initial positions, and determining the dipole parameters by a non-linear search that minimizes differences between the field computed from the dipole model, and that which is measured. The ECD procedure is sensitive to the noise and the correct offset removal. The noise is usually reduced by event-related time averaging.

More general solutions without an a priori assumption about the source distribution can be obtained by minimum norm methods, first proposed for MEG in Ref. [24]. This inverse problem is under-determined, solutions are diffuse, and, unweighted minimum norm favors solutions close to the sensors.

3.3. MEG inversion methods which also contribute to noise cancellation

The methods listed in Table 1 (panel c) generally operate in a multi-dimensional signal space with dimension equal to the number of sensors. In such a space, the angle between the vectors corresponding to different sources is large and it is possible to extract the desired activity while suppressing noise or activity from unwanted regions.

A general representative of this family of solutions is a beamformer [25–29]. Assume that the MEG measurement can be modeled by fixed and uncorrelated multiple dipoles in a homogeneous spherical conducting medium, and that only tangential sources contribute to the signal. First, consider the linearly constrained minimum variance beamformer (LCMV). A dipole at a position θ can be decomposed into two arbitrarily oriented but orthogonal components $\boldsymbol{q}_{\theta 1}$ and $\boldsymbol{q}_{\theta 2}$. The forward solutions per unit dipole for the two components, $\boldsymbol{B}_{\theta 1}$ and $\boldsymbol{B}_{\theta 2}$, can be combined into a gain matrix $\boldsymbol{H}_\theta = [\boldsymbol{B}_{\theta 1}, \boldsymbol{B}_{\theta 2}]$. Let the vector $\boldsymbol{m}(t)$ represents an instantaneous measurement. Define a spatial filter on location θ as $y_\theta(t) = \boldsymbol{W}_\theta^{\mathrm{T}} \boldsymbol{m}(t)$, where $\boldsymbol{W}_\theta$ is the weight matrix, determined by minimizing the power projected from location θ, $P_\theta = \boldsymbol{W}_\theta^{\mathrm{T}} \boldsymbol{C} \boldsymbol{W}_\theta$, subject to the unity gain condition, $\boldsymbol{W}_\theta^{\mathrm{T}} \boldsymbol{H}_\theta = \mathbf{I}$, where $\boldsymbol{C}$ is the covariance matrix of the measurement and $\boldsymbol{I}$ is the identity matrix. The weights are given as [26]

$$\boldsymbol{W}_\theta = \boldsymbol{C}^{-1} \boldsymbol{H}_\theta (\boldsymbol{H}_\theta^{\mathrm{T}} \boldsymbol{C}^{-1} \boldsymbol{H}_\theta)^{-1}. \tag{2}$$

The weights can be used to compute the time course of the dipole magnitude variation, $y_\theta(t)$, or the local power P_θ, or the power normalized by the noise projected by the beamformer, $Z_\theta = P_\theta / N_\theta$, where $N_\theta = \boldsymbol{W}_\theta^{\mathrm{T}} \Sigma \boldsymbol{W}_\theta$, and Σ is the sensor noise covariance matrix. A spatial image of the brain activity can be obtained by scanning the beamformer through the region of interest (3-D search).

Another approach is to construct a beamformer where at each 3-D location the power is probed only along a specified direction. This direction is rotated in the tangential plane and the orientation at which either P_θ or Z_θ is maximized corresponds to the solution for that location. The location indicator θ is 4-D, i.e., three spatial coordinates and one orientation and the approach is called synthetic aperture magnetometry (SAM) [27]. By retaining only one vector in the gain matrix, $\boldsymbol{H}_\theta = \boldsymbol{B}_\theta$, the SAM weights are obtained as $\boldsymbol{W}_\theta = \boldsymbol{C}^{-1} \times \boldsymbol{B}_\theta / \boldsymbol{B}_\theta^{\mathrm{T}} \boldsymbol{C}^{-1} \boldsymbol{B}_\theta$. The dependence of the SAM Z_θ on the probing orientation is shown in Fig. 5 for three different source magnitudes. For high signal-to-noise ratio (SNR), the Z_θ exhibits a sharp peak accurately oriented along the dipole. For decreasing SNR, the Z_θ peak is broadening and moving slightly away from the correct dipole orientation.

The SAM and LCMV responses can be computed analytically for one or two dipoles in random noise if the geometry is axially symmetrical and the sensor density is high [28]. Also, it has been shown analytically, by simulation, and on real data that the SAM peak width is narrower by $\sqrt{2}$ than the LCMV peak width. Thus, eventhough SAM is more computationally intensive, it produces better spatial resolution.

The character of the SAM solutions is illustrated in Fig. 6. The projected power P_θ and noise

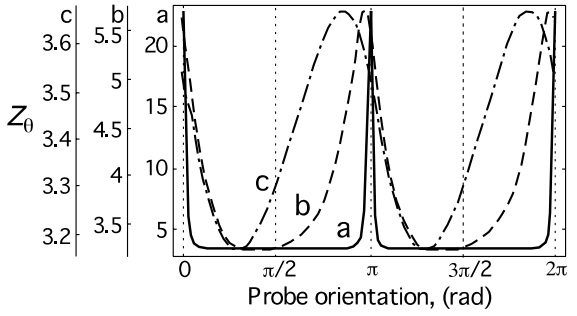

Fig. 5. SAM Z_θ response to a rotating probe positioned on a dipole source. Brain noise simulated by 1000 randomly positioned and randomly oriented dipoles within a spherical shell between 6 and 8 cm radii. Dipole on x_3 axis, oriented along x_1 axis, distance from the model sphere center $a = 5$ cm, sensor shell radius $r = 11.5$ cm, 162 channels, sensor white noise density $v_w = 3$ fT rms/$\sqrt{\text{Hz}}$, $BW = 15$ Hz, no regularization. (a) $q = 100$ nA m; (b) $q = 20$ nA m; (c) $q = 5$ nA m.

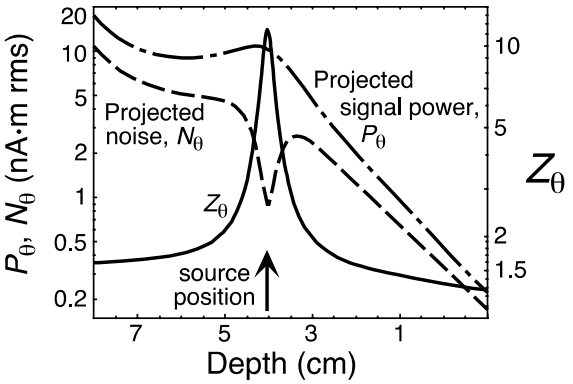

Fig. 6. SAM depth profiles through a dipole for P_θ, N_θ, and Z_θ. Conducting sphere radius $r = 9$ cm, dipole distance from the sphere center $a = 5$ cm (depth = 4 cm).

N_θ exhibit a peak and a dip directly above the dipole, however, as the probing voxel approaches the model sphere center, both P_θ and N_θ diverge because $\boldsymbol{B}_\theta \to 0$. The singularity at the sphere center is the same for P_θ and N_θ, and is removed when Z_θ is computed. Note that Z_θ exhibits a sharp maximum above the dipole and its shape is mostly determined by the projected noise.

The SAM weights are determined for a given target voxel θ and the existing interference sources. The sensitivity at a location 'A' can then be computed as $\boldsymbol{W}_\theta^{\mathrm{T}} \boldsymbol{B}_A$ and is shown in Fig. 7 for three interference sources (circles) and a target voxel (square). To suppress the interference sources, the beamformer projects nulls close to them (white curves in Fig. 7). Fig. 7a–c shows how the nulls reconfigure when the target voxel position changes. The closeness of the nulls to the interferers depends on SNR. For decreasing SNR, the nulls move away from the interferers and the interferer power starts leaking into the SAM output.

When the noise and signal vectors are nearly parallel, SAM and other beamformers can project large sensor noise. To reduce it, the beamformers can be regularized, i.e., the covariance matrix in Eq. (2) can be replaced by $\boldsymbol{C} + \mu v^2 \boldsymbol{I}$, where μ is a regularization constant and v is the sensor rms noise. The regularization, however, also reduces the spatial selectivity and in fact a completely regularized SAM ($\mu \to \infty$) is equivalent to signal space projection (SSP), where the measurement

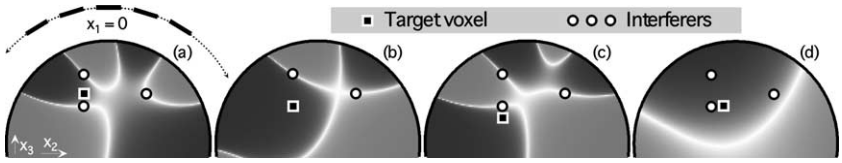

Fig. 7. SAM sensitivity patterns. The SAM weights were determined for the indicated target voxel and interference sources. $M = 100$ channels, sensor shell radius $r = 10.7$ cm, conducting sphere radius $r_{\mathrm{sph}} = 8$ cm, $v_{\mathrm{w}} = 3$ fT rms/$\sqrt{\mathrm{Hz}}$, $BW = 15$ Hz, no brain noise. Interferers: $q_1 = 35$ nA m at (0, −2, 5.5), $q_2 = 120$ nA m at (0, −2, 3), $q_3 = 50$ nA m at (0, 3, 4), all perpendicular to the figure plane. Origin at the sphere center. (a, b, c) Weights computed by unregularized SAM; (a) target at (0, −2, 4) cm; (b) target at (0, −2, 3) cm; (c) target at (0, −2, 2) cm; (d) fully regularized SAM (SSP) for target at (0, −1, 3) cm.

vector is simply projected to the signal space direction of interest. Poor spatial resolution of a fully regularized SAM is illustrated in Fig. 7d, where the signals from interferers and the target voxel are all in the region of high beamformer sensitivity.

Beamformers are sensitive to the signal space direction defined by the forward solution $\boldsymbol{B}_\theta$ in Eq. (2). If the real forward solution is different from the assumed one, the beamformer will perform poorly. This is illustrated in Fig. 8 for the SAM response to extended and point sources. The extended source is 1 cm long and consists of 50 correlated and aligned dipoles. For small SNR, the SAM response to the two source types is roughly the same, because their signal space vectors are smeared by noise and are not distinguishable. When the SNR increases, the two vectors become distinct, and the SAM response to the extended source decreases, while that to the point source increases. Similarly, the beamformers also fail to detect two correlated point sources if the separation between their signal vectors is above the noise.

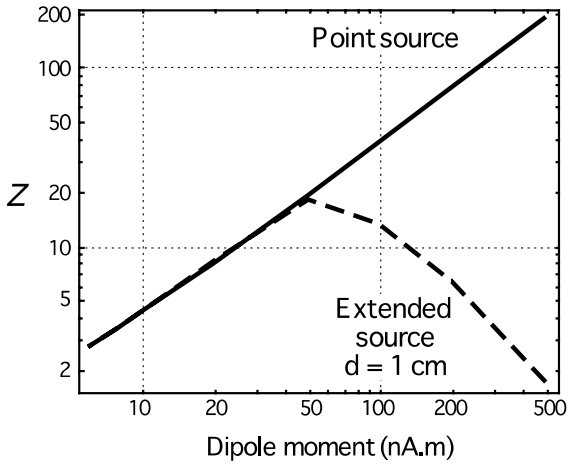

Fig. 8. SAM sensitivity to extended and point sources. $M = 162$ channels, a spherical shell extending from the vertex to $3\pi/4$, an extended or a point source located on the x_3 axis at a distance of $a = 6$ cm from the model sphere center and oriented along the x_1 axis. Extended source length $d = 1$ cm (50 collinear equally-spaced dipoles), magnitudes of the extended and the point sources are equal.

The difference between the point and extended sources would not be detected by a dipole fit, because the normalized difference of their squared fields is less than about 0.3% for the whole range of possible depths.

Multiple signal classification (MUSIC) [30] is a subspace scanning method related to the beamformers. MUSIC determines the dipole parameters by requiring that the dipole forward solution be orthogonal to the noise subspace. In the limit of high SNR, the SAM and MUSIC results are similar [28]. Note that unaveraged MEG signals do not have a noise subspace.

The principal component analysis (PCA), e.g., [31] and independent component analysis (ICA), e.g., [32], methods also find vectors in signal space which are representative of the required solutions. The PCA method utilizes the orthogonal singular spatial vectors and the ICA method assumes that the sources are statistically independent and it determines the source vectors by optimizing a scalar measure of some distributional property based on entropy, mutual independence, high order decorrelation, etc.

Methods based on non-linear dynamics can also be successfully used for separation of lower-dimensional MEG signal from complex signals, e.g., [33].

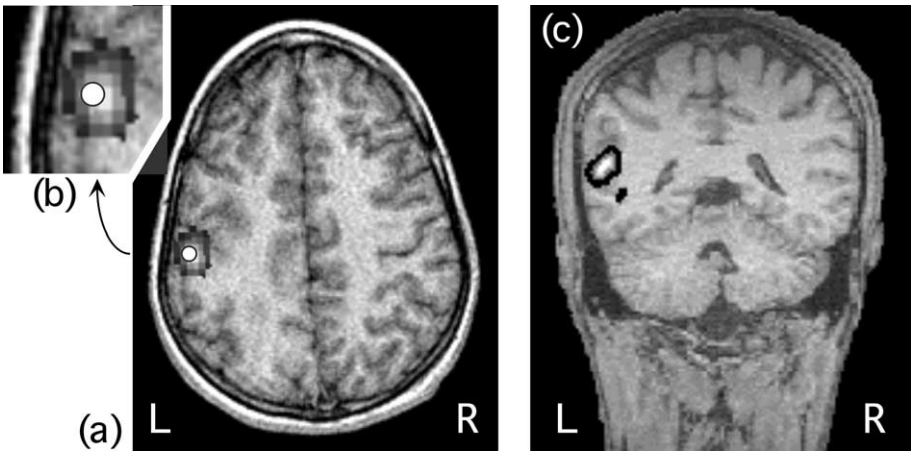

Fig. 9. Examples of SAM results. (a, b) SAM and dipole analyses of SEF, electrical stimulation of right median nerve. The dipole is represented by a black-rimmed white dot overlaid on the SAM result. Courtesy of Drs. D. Cheyne and S.E. Robinson; (c) SAM image showing a region of brain activated during auditory hallucinations in schizophrenia, adapted from Ref. [34].

4. Examples of MEG results

An example of somatosensory evoked fields (SEF) analysis by SAM is shown in Fig. 9. Unaveraged signals were analyzed by SAM and are superposed on MRI slice in Fig. 9a and b. The data were also averaged and the feature at 50 ms after stimulus (P50) was fitted by a single dipole (3.5% fit error). The dipole fit and the active region outlined by SAM are in a good agreement.

Analysis by SAM T-statistics of brain activation during auditory hallucinations in schizophrenia is shown in Fig. 9c. The subject could distinguish between the normal and hallucinogenic states and was asked to press a button when the hallucinations stopped [34]. Eight repetitions were available and the statistics was computed using a bootstrap method (jack-knife). Only SAM values with high significance ($p < 10^{-3}$) are shown.

5. Conclusions

Weak MEG signals, measured in the presence of large environmental and body-generated noise, are usually interpreted by solving for the current sources. However, the large noise and non-unique and ill-defined solution pose significant challenges to MEG source localization. These obstacles can be overcome by effective noise cancellation and by spatially selective MEG localization methods. It was shown that synthetic noise cancellation in combination with moderately shielded rooms can provide noise attenuation in excess of 10^7. In addition, MEG localization methods based on spatial filtering provide good resolution and attenuation of the background clutter. Thus the seemingly impossible task of extracting useful information from tiny MEG signals in large noise is resolved, and even sources of spontaneous activity can be successfully localized.

Acknowledgements

I would like to thank Dr. S.E. Robinson for numerous stimulating discussions related to the material in this paper and Dr. A.A. Fife for comments and careful reading of the manuscript.

References

[1] H. Berger, Arch. Psychiat. Nervenkr. 7 (1929) 527.
[2] D. Cohen, Science 161 (1968) 784.
[3] R. Jaklevic, R.C. Lambe, A.H. Silver, J.E. Mercereau, Phys. Rev. Lett. 12 (1964) 159.
[4] J.E. Zimmerman, A.H. Silver, Phys. Lett. 10 (1964) 47.
[5] D. Cohen, Science 175 (1972) 664.

[6] J. Vrba, K. Betts, M.B. Burbank, et al., IEEE Trans. Appl. Supercond. 3 (1993) 1878.
[7] K.E.T. Knuutila, A.I. Ahonen, M.S. Hamalainen, et al., IEEE Trans. Mag. 29 (1993) 3315.
[8] S.E. Robinson, M.B. Burbank, A.A. Fife, et al., in: J. Nenonen, et al. (Eds.), Biomag2000, Proc. 12th Int. Conf. on Biomagnetism, Helsinki Univ. of Technology, Espoo, Finland, 2001, pp. 919–922.
[9] J.P. Wikswo Jr., in: S.J. Williamson, et al. (Eds.), Advances in Biomagnetism, Plenum Press, New York, 1989, pp. 1–18.
[10] M. Hamalainen, R. Hari, R.J. Ilmoniemi, et al., Rev. Modern Phys. 65 (1993) 413.
[11] R.L. Fagaly, in: S. Sato (Ed.), Advances in Neurology, vol. 54, Magnetoencephalography, New York, Raven Press, 1990, pp. 11–32.
[12] H. Helmholtz, Ann. Phys. Chem. 89 (1853) 211 and 353.
[13] C. Bertrand, M. Ohmi, R. Suzuki, H. Kado, IEEE Trans. Biomed. Eng. 48 (2001) 533.
[14] J.E. Zimmerman, J. Appl. Phys. 48 (1977) 702.
[15] Vacuumschmelze GmbH, Hanau, Germany; Shielded Room model AK-3.
[16] J. Bork, H.-D. Hahlbohm, R. Klein, A. Schnabel, in: J. Nenonen, et al. (Eds.), Biomag2000, Proc. 12th Int. Conf. on Biomagnetism, Helsinki Univ. of Technology, Espoo, Finland, 2001, pp. 970–973.
[17] H. Matsuba, K. Shintomi, A. Yahara, et al., in: C. Baumgartner, et al. (Eds.), Biomagnetism: Fundamental Research and Clinical Applications, Elsevier, IOS Press, 1995, pp. 483–489.
[18] J. Vrba, in: H. Weinstock (Ed.), SQUID Sensors: Fundamentals, Fabrication and Applications, Kluwer, Dordrecht, 1996, pp.117–178.
[19] D. Drung, in: H. Koch, H. Lubbig (Eds.), SQUID'91, Superconducting Devices and their Applications, Springer Proceedings in Physics 64 (1991) 542.
[20] W. Becker, V. Dickmann, R. Jurgens, C. Kornhuber, Physiol. Meas. 14 (1993) A45.
[21] V.O. Kelha, J.M. Pukki, R.S. Peltonen, et al., IEEE Trans. Magn. 18 (1982) 260.
[22] H.J.M. ter Brake, H.J. Wieringa, H. Rogalla, Meas. Sci. Technol. 2 (1991) 596.
[23] J. Sarvas, Phys. Med. Biol. 32 (1987) 11.
[24] M.S. Hamalainen, R.J. Ilmoniemi, Report TKK-F-A559, Helsinki University of Technology, Espoo, Finland, 1984.
[25] K. Sekihara, B. Scholz, IEEE Trans. Biomed. Eng. 43 (1966) 281.
[26] B.D. Van Veen, W. Van Drongelen, M. Yuchtman, A. Suzuki, IEEE Trans. Biomed. Eng. 44 (1997) 867.
[27] S.E. Robinson, J. Vrba, in: T. Yoshimoto, et al. (Eds.), Recent Advances in Biomagnetism, Tohoku University Press, Sendai, 1999, pp. 302–305.
[28] J. Vrba, S.E. Robinson, in: M.B. Mathews (Ed.), Proc. 34th Asilomar Conf. on Signals, Systems, and Computers, IEEE Omnipress, vol. 1, 2000, pp. 313–317.
[29] K. Sekihara, S.S. Nagarajan, D. Poeppel, A. Marantz, Y. Miyashita, IEEE Trans. Biomed. Eng. 48 (2001) 760.
[30] J.C. Mosher, P.S. Lewis, R.M. Leahy, IEEE Trans. Biomed. Eng. 39 (1992) 541.
[31] J. Maier, G. Dagnelie, H. Spekreijse, B. van Dijk, Vision Res. 27 (1987) 165.
[32] J.-F. Cardoso, Proc. IEEE 86 (1998) 2009.
[33] R. Cawley, G.H. Hsu, Phys. Rev. A 46 (1992) 3057.
[34] R. Ishii, K. Shinosaki, Y. Ikejiri, et al., NeuroReport 11 (2000) 3283.